Nano Research

ISSN 1998-0124 CN 11-5974/O4
https://doi.org/10.1007/s12274-024-6463-2

Catalytic anode surface enabling *in situ* polymerization of gel polymer electrolyte for stable Li metal batteries

Guocheng Li[1,§], Kang Liang[2,§], Yuanjian Li[1], Xiangrui Duan[1], Lin Fu[1], Zhao Cai[3], Zhaofu Zhang[2], Jiangnan Dai[1], and Yongming Sun[1] (✉)

[1] *Wuhan National Laboratory for Optoelectronics, Huazhong University of Science and Technology, Wuhan 430074, China*
[2] *The Institute of Technological Sciences, Wuhan University, Wuhan 430074, China*
[3] *Faculty of Materials Science and Chemistry, China University of Geoscience (Wuhan), Wuhan 430074, China*
[§] *Guocheng Li and Kang Liang contributed equally to this work.*

Received: 12 November 2023 / **Revised:** 28 December 2023 / **Accepted:** 2 January 2024

ABSTRACT

Employing quasi-solid-state gel polymer electrolyte (GPE) instead of the liquid counterpart has been regarded as a promising strategy for improving the electrochemical performance of Li metal batteries. However, the poor and uneven interfacial contact between Li metal anode and GPE could cause large interfacial resistance and electrochemical Li stripping/plating inhomogeneity, deteriorating the electrochemical performance. Herein, we proposed that the functional component of composite anode could work as the catalyst to promote the *in situ* polymerization reaction, and we experimentally realized the integration of polymerized-dioxolane electrolyte and Li/$Li_{22}Sn_5$/LiF composite electrode with low interfacial resistance and good stability by *in situ* catalyzation polymerization. Thus, the reaction kinetics and stability of metallic Li anode were significantly enhanced. As a demonstration, symmetric cell using such a GPE-Li/$Li_{22}Sn_5$/LiF integration achieved stable cycling beyond 250 cycles with small potential hysteresis of 25 mV at 1 mA·cm^{-2} and 1 mAh·cm^{-2}, far outperforming the counterpart regular GPE on pure Li. Paired with $LiNi_{0.5}Co_{0.3}Mn_{0.2}O_2$, the full cell with the GPE-Li/$Li_{22}Sn_5$/LiF integration maintained 85.7% of the original capacity after 100 cycles at 0.5 C (1 C = 200 mA·g^{-1}). Our research provides a promising strategy for reducing the resistance between GPE and Li metal anode, and realizes Li metal batteries with enhance electrochemical performance.

KEYWORDS

catalyzation polymerization, interface resistance, interfacial stability, Li metal batteries, electrochemical performance

1 Introduction

Li metal anode has gained great attention owing to its high specific capacity (3860 mAh·g^{-1}) and low redox potential (–3.04 V versus standard hydrogen electrode (SHE)) for achieving next-generation rechargeable batteries with high energy density [1, 2]. However, the thermodynamical instability between conventional liquid electrolyte and metallic Li could lead to parasitic reactions between them, and the large volume change of metallic Li anode could cause continuous electrolyte-metallic Li interphase evolution, which leads to electrochemical performance degradation [3]. More seriously, Li dendrites could be produced during the repeated Li plating/stripping processes in regular carbonate liquid electrolyte and could pierce the porous polymer separator, which, together with the high chemical instability and flammability of liquid electrolyte, could cause safety concerns of batteries [4].

Solid electrolytes have been recently extensively investigated as promising alternatives for the liquid electrolytes due to their better thermal stability and positive effect in suppressing the growth of metallic Li dendrites [5, 6]. Preliminary success has been widely shown in battery prototypes using both inorganic and polymer solid electrolytes, featuring extended cycling life and better thermal safety [7]. Benefited by their soft feature, polymer solid electrolytes could enable better contact with the metallic Li anode, and demonstrate potentially low interphase resistance [8]. It could also facilitate the formation of a mechanically robust electrolyte-metallic Li interphase with high stability, which quite differs from some rigid inorganic counterparts, such as the oxide ceramic solid electrolyte [9]. Very recently, *in situ* polymerization of gel polymer electrolyte (GPE) with the assistance of catalysts (e.g., cationic aluminum species, tris(pentafluorophenyl) borane, lithium bis(trifluoromethane)sulfonimide (LiTFSI), lithium difluoro(oxalato)borate, and lithium hexafluorophosphate ($LiPF_6$)) and heat treatment becomes an important research direction due to the good compatibility with the current battery manufacture and high ionic conductivity and high Li^+ transference number of these polymer electrolytes [10–14]. However, a significant challenge that may hinder the practical implantation of GPE lies its inferior contact with pure Li metal anode due to the inferior consistency of metal and polymer, and relatively high interphase resistance, which could deteriorate the electrochemical performance [15]. The large volume change of pure Li metal anode during the charge/discharge processes would certainly further aggravate the contact degradation between the anode and regular GPE and yield a porous and thickened reaction layer, speeding up the battery failure (Fig. 1(a)) [16]. Construction of Li

---

Address correspondence to yongmingsun@hust.edu.cn

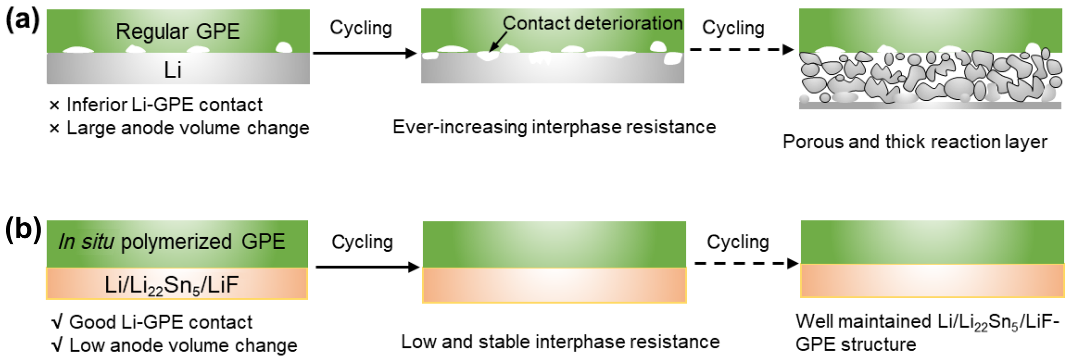

Figure 1 (a) Schematic illustration for structural evolution of pure Li metal electrode with regular GPE on Li stripping/plating cycling. (b) Schematic illustration for good structural stability of $Li/Li_{22}Sn_5/LiF$ composite anode using *in situ* polymerized GPE on the anode surface on Li stripping/plating cycling.

metal composite electrode was evidenced as an effective strategy to extend the cycle life and suppress the Li dendrite formation by accommodating the drastic volume variation and regulating the Li plating/stripping behavior [17]. Specifically, migration of ions and electrons and uniform electrochemical Li plating/stripping behavior can be synchronously facilitated in Li alloy (e.g., $Li_{22}Sn_5$, $Li_{23}Sr_6$, $Li_{1.95}Mg$, Li_9Al_4, and Li_5B_4)-based Li metal composite anodes due to the hybrid electronic and ionic conductivity and their strong affinity to metallic Li [18–21].

Herein, we proposed the design of composite Li metal foil that can *in situ* catalyze the polymerization of GPE, which could synchronously eliminate the anode volume change and realize low interphase resistance between electrolyte and anode on charge/discharge cycling processes. Composite $Li/Li_{22}Sn_5/LiF$ foil anode was fabricated via a mechanical kneading approach using SnF_2 and metallic Li as the raw materials. The residual SnF_2 nanoparticles catalyzed the *in situ* polymerization of dioxolane (DOL) on the anode surface with close contact and low interphase resistance. Together with the hybrid conductive $Li_{22}Sn_5$ framework and protective LiF component, the good electrode/GPE integrity and stable electrode structure with compact and thin reaction layer were achieved over long-term electrochemical cycling (Fig. 1(b)). Consequently, the $Li/Li_{22}Sn_5/LiF$ symmetric cell achieved stable cycling performance over 500 h with a low overpotential of 25 mV. Paired with a $LiNi_{0.5}Co_{0.3}Mn_{0.2}O_2$ (NCM) electrode, the full cell demonstrated a remarkable capacity retention of 85.7% for 100 cycles at 0.5 C within the potential range of 2.8–4.3 V.

2 Experiment section

2.1 Synthesis of $Li/Li_{22}Sn_5/LiF$ and GPE

$Li/Li_{22}Sn_5/LiF$ composite electrode was fabricated by repeated mechanical kneading operations using Li foil (99.95%, China Energy Lithium) and SnF_2 powder (99%, Sigma) in the argon glove box (< 1 ppm H_2O and O_2) according to our previous publication [17]. For the fabrication of regular GPE on the surface of pure Li electrode, 2 M $LiPF_6$ was dissolved into the liquid precursor electrolyte (1 M LiTFSI in DOL/1,2-dimethoxyethane (DME)). The obtained uniform solution was then spontaneously transformed into GPE within the sealed cell after resting for 12 h [13]. *In situ* formed GPE was prepared via initiating the ring-opening polymerization of the liquid precursor electrolyte by the residual SnF_2 nanoparticles on the surface of the as-designed composite $Li/Li_{22}Sn_5/LiF$ foil in the sealed cell.

2.2 Material characterization

Scanning electron microscopy (SEM) for samples was performed using a GeminiSEM300 field-emission scanning electron microscopy under an acceleration voltage of 5 kV. The molecular structures of the liquid electrolyte and the obtained GPE were studied using Fourier transform infrared (FTIR) spectroscopy on a Nicolet iS50R FTIR spectrometer. Raman characterizations were conducted using a confocal LabRAM HR800 Raman micro-spectrometer (HORIBA).

2.3 Electrochemical measurement

The NCM electrodes were prepared by mixing the active materials, Super P, and polyvinylidene fluoride (PVDF) at a weight ratio of 90:5:5 in N-methyl pyrrolidone (NMP) and casting the slurry onto an Al foil. After drying in a vacuum oven at 80 °C for 8 h to remove NMP solvent, the cathodes were cut for cell assembly. The mass loading of NCM cathode was about 4.0 $mg \cdot cm^{-2}$. CR-2032 coin-type cells were assembled in the argon glove box using Celgard 2300 as the separator, and the liquid precursor electrolyte (1 M LiTFSI in DOL/DME) or *in situ* obtained GPE as the electrolytes. 70 μL liquid precursor electrolyte (1 M LiTFSI in DOL/DME) was used in each coin-type cell. Galvanostatic charge/discharge measurements of cells were performed using LAND CT2001A testing instruments. A Biologic VMP3 electrochemistry workstation was employed for electrochemical impedance spectroscopy (EIS) and linear sweep voltammetry (LSV) measurements.

2.4 Simulation

COMSOL Multiphysics software with Li battery module was employed to simulate the distribution of Li^+ concentration and voltage of the cell with $Li/Li_{22}Sn_5/LiF$-GPE and Li-GPE integration, respectively. The Li^+ concentration was 1 M and the ionic conductivity of the electrolyte was 1 $mS \cdot cm^{-1}$. The simulation was conducted in a 10 μm × 10 μm half-cell electrodeposition system.

3 Results and discussion

SnF_2 and Li metal foil were used as the raw materials to fabricate the $Li/Li_{22}Sn_5/LiF$ composite electrode with a mechanical kneading approach at room temperature (Fig. S1 in the Electronic Supplementary Material (ESM)) [17]. Residual SnF_2 nanoparticles existed and were distributed over the entire electrode surface (Fig. 2(a), and Figs. S2 and S3 in the ESM). As a highly efficient catalyzer, SnF_2 could *in situ* initiate the ring-opening polymerization of DOL near the electrode surface, and transform the liquid precursor electrolyte (1 M LiTFSI in DOL/DME, 1:1 by volume) into the GPE (Fig. 2(b) and Fig. S4 in the ESM) [16]. The remaining DME solvent was uniformly mixed with the GPE as a plasticizer. It should be noted that $Li_{22}Sn_5$ and LiF in the composite anode are incapable of catalyzing the *in situ* polymerization of DOL on the anode surface (Fig. S5 in the ESM). Figure 2(c) illustrates the polymerization reaction mechanism of

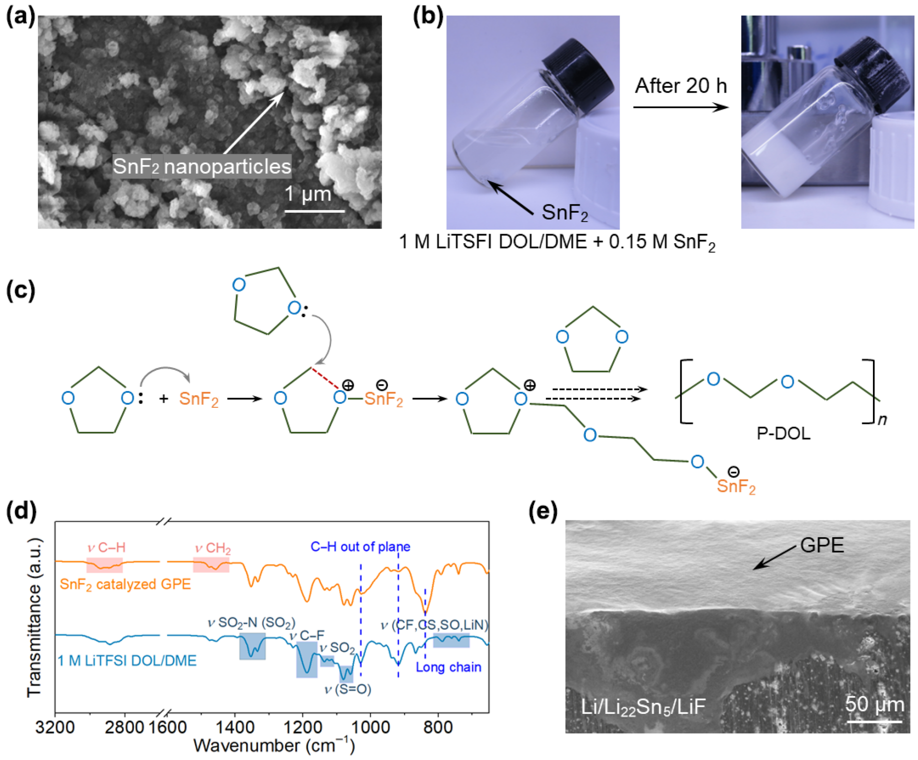

Figure 2 (a) SEM image of the residual SnF_2 nanoparticles on the surface of the $Li/Li_{22}Sn_5/LiF$ composite electrode. (b) Optical photos of 1 M LiTFSI in DOL/DME (1:1 by volume) with 0.15 M SnF_2 powder before and after resting 20 h. (c) Reaction mechanism for SnF_2 catalyzing DOL polymerization. (d) FTIR spectra of the liquid precursor electrolyte (1 M LiTFSI in DOL/DME) and SnF_2 catalyzed GPE. (e) SEM image of $Li/Li_{22}Sn_5/LiF$ composite electrode with GPE via catalyzing DOL polymerization on its surface.

DOL initiated by SnF_2 catalyzer. As known as a Lewis acid, the electropositive Sn atom in SnF_2 attaches to the O atom in monomer DOL and strongly interacts with it, which renders an electropositive center on the O atom and an increased electropositive of the nearby C atom because of the electron-withdrawing effect [16]. Following that, the electronegative O atom from another monomer DOL attacks the electropositive increased C atom and breaks the C–O bond (marked in Fig. 2(c)), and initiates the ring-opening polymerization of monomer DOL in the liquid precursor electrolyte. After many repeated cationic polymerization of monomer DOL, the chain of polymer continues to increase and yields the ultimate solid polymerized-DOL (P-DOL). FTIR spectroscopy spectra in Fig. 2(d) confirmed the successful polymerization of monomer DOL. For SnF_2 catalyzed GPE, the signal of C–H out of plane from monomer DOL almost disappeared, and the vibration of long chain belong to P-DOL emerged [10]. To further validate the *in situ* polymerization of GPE with residual SnF_2 catalyzer from composite electrode, SEM was conducted. A flat solid polymer layer transformed from the liquid precursor electrolyte was observed tightly covered the electrode surface after resting (Fig. 2(e)).

Given the low viscosity of precursor electrolyte and ubiquitous residual SnF_2, a close interfacial contact between GPE and composite electrode was realized (Fig. 3(a)). For a comparison, 2 M $LiPF_6$ dissolved in the bulk of liquid precursor was chosen as the catalyzer to initiate the polymerization of DOL on the surface of the pure Li metal electrode (Figs. S6 and S7 in the ESM). As a note, 2 M $LiPF_6$ additive with high concentration of Li salts significantly increased the electrolyte viscosity, which reduced the wettability of the electrolyte to the electrode, rendering a poor interfacial contact between the pure Li electrode and the as-produced GPE (Fig. 3(b) and Fig. S8 in the ESM) [22]. To investigate the interfacial contact between different Li metal electrodes and GPE, Li||Li and $Li/Li_{22}Sn_5/LiF||Li/Li_{22}Sn_5/LiF$ symmetric cells were assembled and subjected to subsequent EIS measurements after the complete conversion of liquid monomer DOL into solid P-DOL. The EIS spectra and corresponding fitting results demonstrated that the interfacial resistance (R_i) for the $Li/Li_{22}Sn_5/LiF||Li/Li_{22}Sn_5/LiF$ symmetric cell was 163 Ω, which was about half of that (316 Ω) for the Li||Li (Figs. 3(c)–3(e), and Fig. S9 and Table S1 in the ESM). Lower interfacial resistance for the $Li/Li_{22}Sn_5/LiF||Li/Li_{22}Sn_5/LiF$ symmetric cell arose from enhanced interfacial contact between $Li/Li_{22}Sn_5/LiF$ electrode and GPE due to the SnF_2 catalytic polymerization effect. The top-view SEM image of the $Li/Li_{22}Sn_5/LiF$ electrode with GPE from the disassembled cell confirmed the even distribution of GPE across the surface of the $Li/Li_{22}Sn_5/LiF$ and the good contact between them (Fig. 3(f)). In contrast, it was observed that GPE was randomly distributed on the surface of the pure Li electrode with uncovered region, supporting the inferior contact between GPE and the anode (Fig. 3(g)). The smaller contact angle of GPE on the $Li/Li_{22}Sn_5/LiF$ electrode than that on the pure Li electrode confirmed the enhanced interfacial affinity between composite electrode and the SnF_2-*in situ* catalyzation produced GPE (Fig. 3(h)). The aforementioned results indicated that component with catalytic effect on the surface of the $Li/Li_{22}Sn_5/LiF$ composite electrode enabled a close interfacial contact with the as-obtained GPE, which could significantly reduce the interphase resistance and lead to potential opportunities for enhancing the homogeneity of electrochemical Li stripping/plating reactions.

To verify the advancement of the $Li/Li_{22}Sn_5/LiF$ electrode with interfacial catalytic polymerized GPE, galvanostatic cyclability results of $Li/Li_{22}Sn_5/LiF||GPE||Li/Li_{22}Sn_5/LiF$ and Li||GPE||Li cells were compared at 1 $mA \cdot cm^{-2}$ and 1 $mAh \cdot cm^{-2}$. GPE for Li||GPE||Li cells was obtained via initiating the ring-opening polymerization of DOL in precursor electrolyte using $LiPF_6$ catalyst, which demonstrated considerable bulk ionic conductivity (~ 1 $mS \cdot cm^{-1}$ at 30 °C), high Li^+ transference number (0.42 and 0.45 for polymerized GPE catalyzed by $LiPF_6$ and SnF_2, respectively) and good flame retardancy (Figs. S10–S12 in the

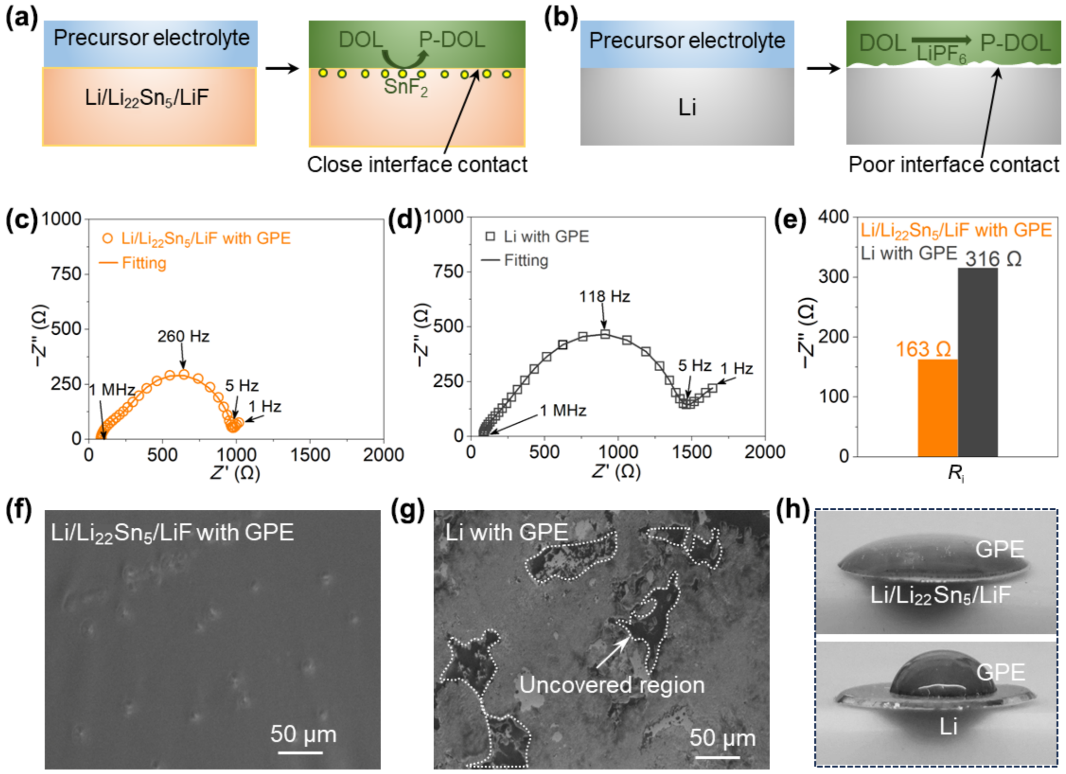

Figure 3 Schematic illustration of the polymerization process of the liquid precursor on the surfaces of (a) the Li/$Li_{22}Sn_5$/LiF and (b) pure Li electrodes. Representative EIS spectra of (c) the Li/$Li_{22}Sn_5$/LiF||GPE||Li/$Li_{22}Sn_5$/LiF and (d) Li||GPE||Li cells. (e) Comparison of the fitted R_i from the representative EIS spectra in (c) and (d). The top-view SEM images of (f) Li/$Li_{22}Sn_5$/LiF and (g) pure Li with GPE from the disassembled cell. (h) Optical photos of the Li/$Li_{22}Sn_5$/LiF and pure Li electrodes with SnF_2 catalyzed GPE and $LiPF_6$ catalyzed GPE, respectively.

ESM). Considering that SnF_2 is present solely on the electrode's surface rather than within the bulk of GPE, the inherent characteristics of the GPE remain unaltered. As depicted in Figs. 4(a) and 4(b), the Li/$Li_{22}Sn_5$/LiF||GPE||Li/$Li_{22}Sn_5$/LiF cell exhibited long-term cycling exceeding 250 cycles, with a stable and minimal hysteresis of 25 mV, significantly surpassing that reported in recent publications (Table S2 in the ESM). In contrast, the Li||GPE||Li counterpart exhibited a larger initial hysteresis of 50 mV and gradual hysteresis augment, indicating the gradual interphase failure and accumulation of undesirable products by parasitic reaction between the pure Li electrode and residual DME solvent in GPE [13]. After 99 cycles, a sudden voltage drop was detected for the Li||GPE||Li cell, suggesting the internal short circuits caused by fast dendritic Li growth. The reduced hysteresis and extended cycling stability were further supported by EIS analysis conducted on symmetric cells after 10 and 50 cycles at 1 $mA \cdot cm^{-2}$ and 1 $mAh \cdot cm^{-2}$. The high-frequency semicircle in the EIS spectra is indexed to the interfacial resistance (from contact interface between GPE and the Li/$Li_{22}Sn_5$/LiF or the pure Li electrodes), and the semicircle at middle-frequency in the EIS spectra stands for the charge-transfer resistance, resulted from the accumulation of nonactive metallic Li and porous reaction layer [23]. After 10 cycles, both electrodes were fully activated accompanied by the collapse of the native oxide layers [24]. For the Li/$Li_{22}Sn_5$/LiF||GPE||Li/$Li_{22}Sn_5$/LiF cell, the interfacial resistance remained at ~ 18 Ω and the charge-transfer resistance slightly increased from 22 to 28 Ω after 50 cycles (Fig. 4(c)). In contrast, the Li||GPE||Li counterpart exhibited rapid increase in both the interfacial resistance (from 18 to 40 Ω) and the charge-transfer resistance (from 30 to 120 Ω) from 10 to 50 cycles (Fig. 4(d)). Even after 100 cycles, the Li/$Li_{22}Sn_5$/LiF||GPE||Li/$Li_{22}Sn_5$/LiF cell delivered values of 30 and 22 Ω for the interfacial resistance and charge-transfer resistance, suggesting the high electrochemical stability of GPE-Li/$Li_{22}Sn_5$/LiF integration upon cycling. However, the total resistance of the Li||GPE||Li cell fell to ~ 0, suggesting the short circuit of the cell (Fig. S13 in the ESM). These results highlighted the significant role of interfacial catalytic polymerization on reducing the interfacial resistance and improving the interfacial stability of Li metal cell with GPE. The *in situ* formed polymer layer could also be well maintained on the surface of the Li/$Li_{22}Sn_5$/LiF composite electrode throughout the cycling process (Fig. S14 in the ESM). It is noteworthy that conductive $Li_{22}Sn_5$ framework in Li/$Li_{22}Sn_5$/LiF was helpful for facilitating Li^+ transport and homogenizing the Li^+ flux, and buffering the volume change of Li metal electrode, thus enabling reduced the potential hysteresis upon repeated Li stripping/plating process and enhanced the structural stability. In addition, protective LiF component could significantly improve anticorrosive property of composite electrode against GPE, guaranteeing a long-term cycling stability. The synergistic effect of interfacial catalytic polymerization and the advantageous $Li_{22}Sn_5$/LiF species was also corroborated by the significantly reduced hysteresis observed in the Li/$Li_{22}Sn_5$/LiF symmetric cell employing GPE, as compared to that utilizing ex-GPE (Fig. S15 in the ESM).

The topography of Li electrodeposits is an important indicator of cycling stability of electrode. The SEM images in Figs. 4(e) and 4(f) manifested distinctive morphological features of the deposited Li on the surface of the Li/$Li_{22}Sn_5$/LiF and pure Li electrodes. Denser and chunky Li deposition layer was observed on the Li/$Li_{22}Sn_5$/LiF electrode after Li plating at 1 $mA \cdot cm^{-1}$ and 1 $mAh \cdot cm^{-1}$. In sharp contrast, the Li electrodeposits on the pure Li electrode consisted of loose and dendritic Li under the same text condition, which could result in significant Li inventory loss for the formation of solid electrolyte interface (SEI) and nonactive metallic Li, the so-called dead Li [17]. High surface area of the Li deposits is recognized as one main factor that accounts for severe Li/electrolyte reaction. As revealed in Fig. 4(g) and Fig. S16(a) in

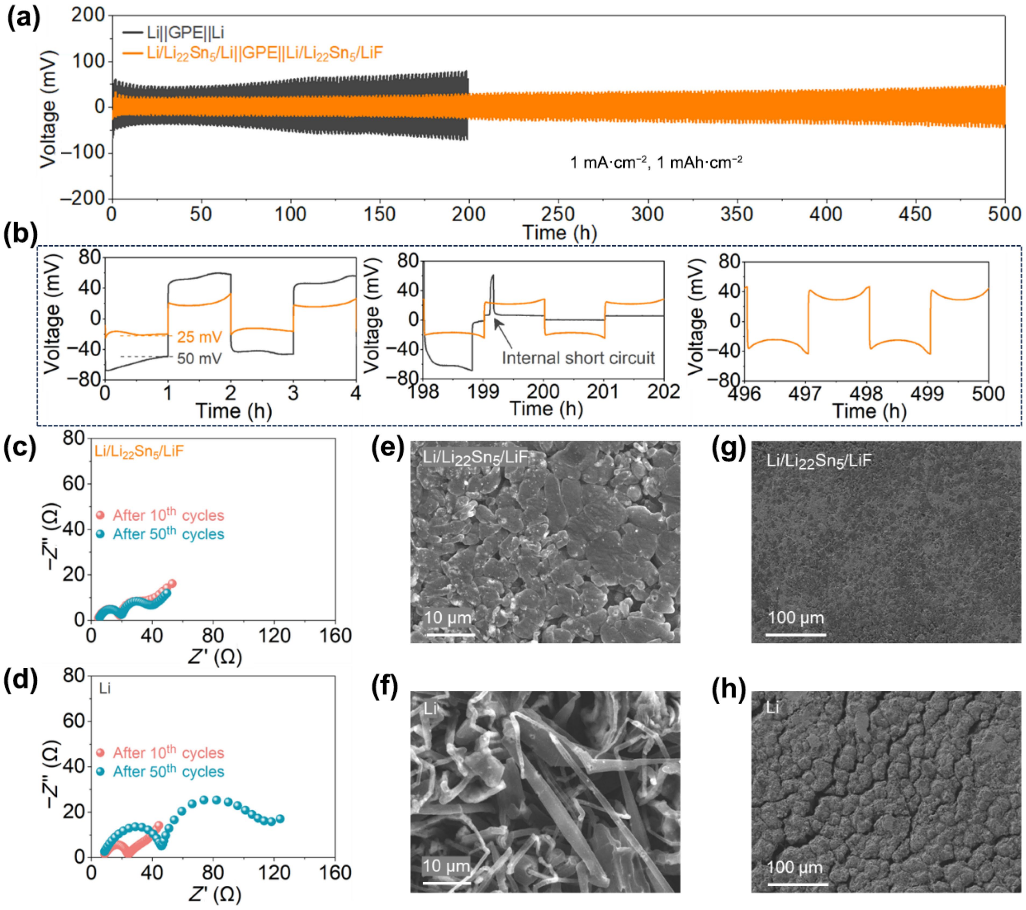

Figure 4 (a) The voltage–time plots and (b) the enlarged profiles at selected times for the Li/$Li_{22}Sn_5$/LiF||GPE||Li/$Li_{22}Sn_5$/LiF and Li||GPE||Li cells cycled at 1 mA·cm^{-2} and 1 mAh·cm^{-2}. Representative EIS spectra of (c) the Li/$Li_{22}Sn_5$/LiF||GPE||Li/$Li_{22}Sn_5$/LiF and (d) Li||GPE||Li cells after 10 and 50 cycles at 1 mA·cm^{-2} and 1 mAh·cm^{-2}, respectively. Top-view SEM images of (e) the Li/$Li_{22}Sn_5$/LiF and (f) pure Li electrodes after Li plating at 1 mA·cm^{-1} and 1 mAh·cm^{-1}, respectively. Top-view SEM images for (g) the Li/$Li_{22}Sn_5$/LiF and (h) pure Li electrodes after 10 cycles at 1 mA·cm^{-2} and 1 mAh·cm^{-2}, respectively.

the ESM, a compact, flat, and thin Li reaction layer was observed for the Li/$Li_{22}Sn_5$/LiF electrode after 10 Li plating/stripping cycles at 1 mA·cm^{-1} and 1 mAh·cm^{-1}, while the pure Li electrode showed a loose, rough, and thick reaction layer containing abundant micrometer-size cracks (Fig. 4(h) and Fig. S16(b) in the ESM).

Finite element simulation was conducted to theoretically understand the mechanisms of Li deposition in Li/$Li_{22}Sn_5$/LiF-GPE integration via monitoring the distribution of Li^+ concentration and potential across the electrode/electrolyte interface using COMSOL Multiphysics 6.0 version [16, 25]. As plotted in Fig. 5(a), compressed Li^+ concentration polarization with uniform Li^+ flux above the vicinity of the composite electrode was observed for the Li/$Li_{22}Sn_5$/LiF-GPE integration. In contrast, Li-GPE integration presented a more uneven incoming Li^+ flux with lower Li^+ concentration at the contact region between Li electrode and the GPE electrolyte (Fig. 5(b)). In the respect of the potential distribution, close interfacial contact between Li/$Li_{22}Sn_5$/LiF and SnF_2-catalyzation produced GPE helped to form a more consistent and homogeneous potential distribution across the electrode than that in the Li-GPE integration (Figs. 5(c) and 5(d)). The cross-sectional Li^+ concentration and potential distribution profiles along X direction at the selected axial distance quantitatively and intuitively demonstrated violent fluctuations across the interface in Li-GPE integration, which would yield hotspots on the surface of Li and lead to the self-enhanced growth of dendritic Li (Figs. 5(e) and 5(f), and Fig. S17 in the ESM) [5]. Note that the disconnected position in curves indicated that the Li^+ concentration and potential were zero due to the presence of voids. However, the Li^+ concentration and potential almost maintained a constant, indicating the capability of homogenizing the Li^+ flux and suppressing the potential aggravation for the Li/$Li_{22}Sn_5$/LiF-GPE integration.

The liquid precursor electrolyte (1 M LiTFSI in DOL/DME, hereinafter referred to LE) usually exhibits improved performance for Li metal anode due to its higher stability against reduction of reactive metallic Li, enabling the formation of flexible oligomers-rich SEI. However, the poor anti-oxidation capability hampers its practical applications in rechargeable Li metal batteries with moderate or high voltage cathodes (e.g., $LiNi_xCo_yMn_{1-x-y}O_2$, $LiCoO_2$, and $LiNi_{0.5}Mn_{1.5}O_4$), as illustrated in Fig. 6(a) [26]. The charge/discharge profile of the NCM||LE||Li cell presented that liquid electrolyte started to be decomposed when the voltage reached to about 3.8 V (Fig. 6(b)). By comparison, GPE could withstand higher voltage of 4.3 V and maintain considerable reversible discharge capacity. As depicted in Fig. S18 in the ESM, the polymerization dramatically widened the oxidative stability to about 4.6 V, obviously higher than 3.8 V for liquid precursor electrolyte. The instability of liquid electrolyte could be attributed to the intrinsic chemical instability against oxidation of liquid DOL, and its polymerization into P-DOL took the responsibility for the widened electrochemical window of obtained GPE [27]. Flowable liquid electrolyte as the precursor of GPE demonstrated good infiltration into the porous NCM cathode electrode (Fig. S19 in the ESM). After resting and full polymerization, the stability of electrolyte against to its oxidation at the cathode side was improved, together with good stability of the Li/$Li_{22}Sn_5$/LiF electrode, the as-fabricated NCM||GPE||Li/$Li_{22}Sn_5$/LiF cell presented impressive electrochemical cyclability, and it delivered reasonably high-capacity retention of 85.7% for 100 cycles at 0.5 C (1 C = 200 mA·g^{-1}) between 2.8 and 4.3 V (Figs. 6(c) and 6(d)).

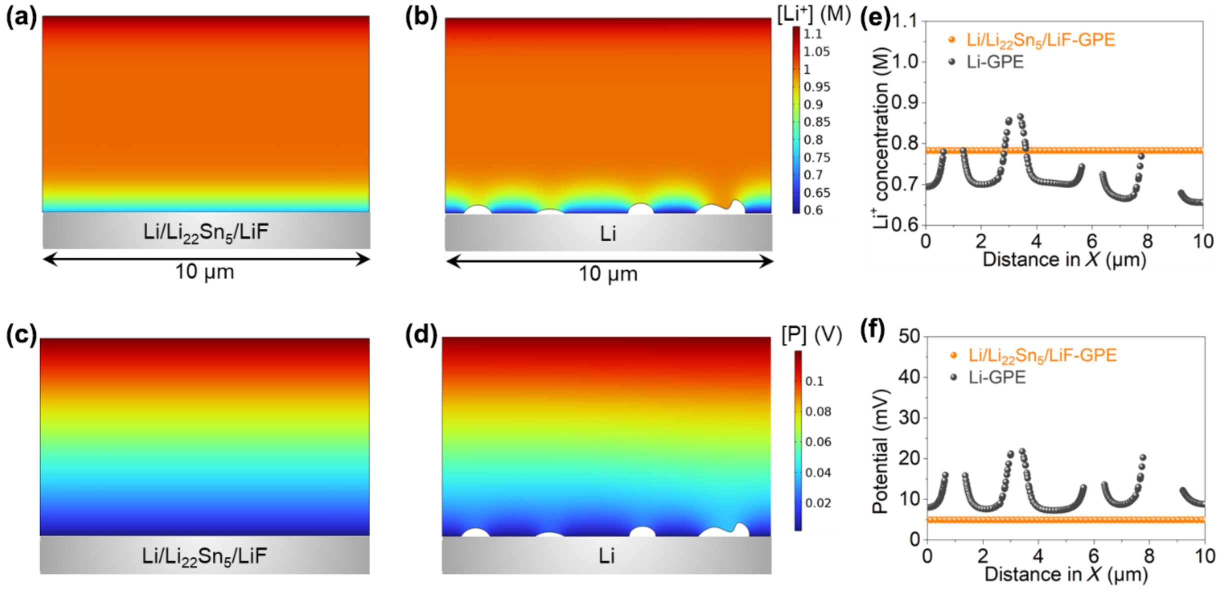

Figure 5 COMSOL Multiphysics simulations of the Li^+ concentration and potential distribution of half cell with ((a) and (c)) the $Li/Li_{22}Sn_5/LiF$-GPE and ((b) and (d)) the Li-GPE integration, respectively. (e) Li^+ concentration and (f) potential distribution profiles at the electrode/electrolyte interface along *X* direction extracted from (a)–(d).

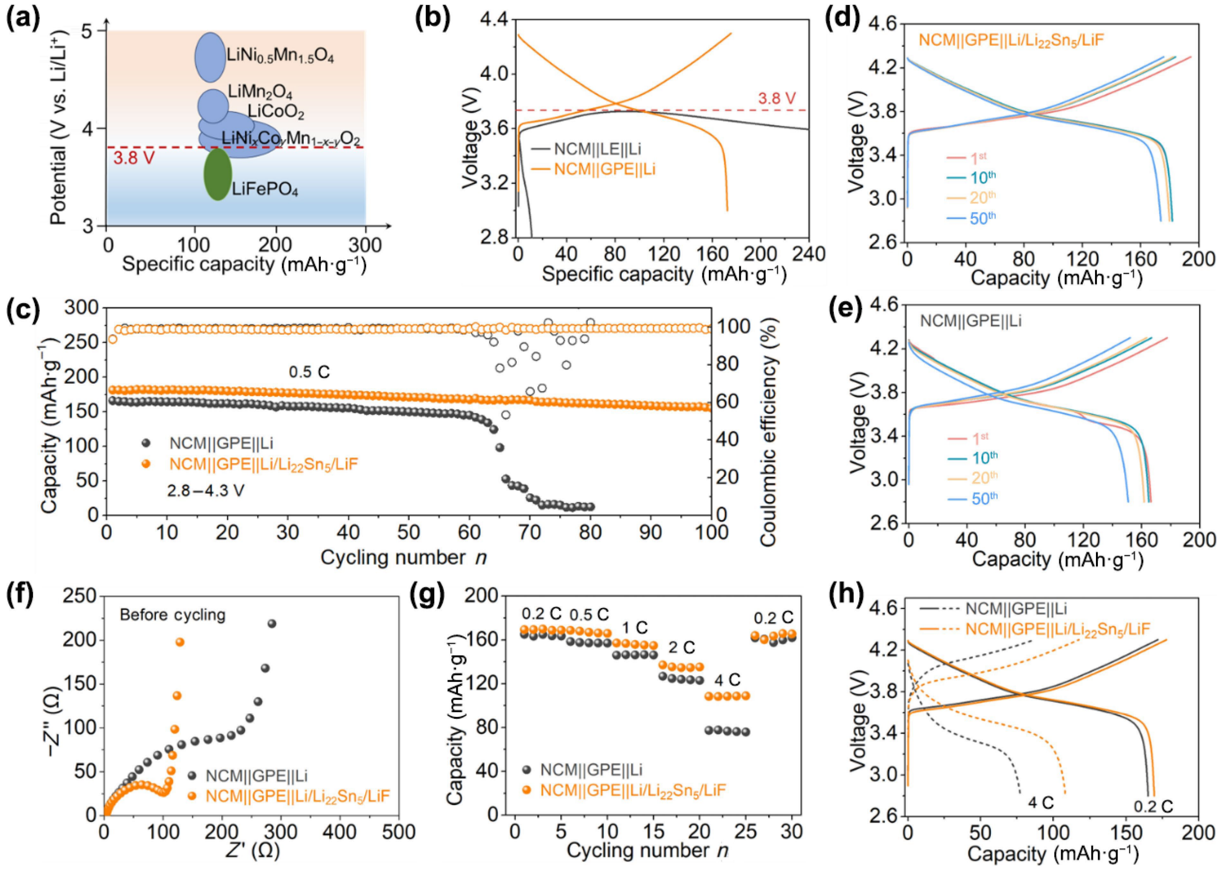

Figure 6 (a) Voltage and specific capacity of various cathode materials. (b) Charge/discharge profiles of the NCM||GPE||Li and NCM||LE||Li cells in the voltage range of 2.8–4.3 V at 0.5 C. (c) Cycling performance of the NCM||GPE||Li and NCM||GPE||$Li/Li_{22}Sn_5/LiF$ cells at 0.5 C. Charge/discharge profiles of (d) the NCM||GPE||$Li/Li_{22}Sn_5/LiF$ and (e) NCM||GPE||Li cells for selected cycles corresponding to (c), respectively. (f) Representative EIS spectra of the NCM||GPE||Li and NCM||GPE||$Li/Li_{22}Sn_5/LiF$ cells before cycling. (g) Rate capability of the NCM||GPE||Li and NCM||GPE||$Li/Li_{22}Sn_5/LiF$ cells. (h) Charge/discharge profiles of the NCM||GPE||$Li/Li_{22}Sn_5/LiF$ and NCM||GPE||Li cells at 0.2 and 4 C, respectively.

Good contact between $Li/Li_{22}Sn_5/LiF$ electrode and GPE with high stability accounted for superior reversibility and small polarization in electrochemical cycling of the NCM||GPE||$Li/Li_{22}Sn_5/LiF$ cell. In contrast, the NCM||GPE||Li cell displayed a sudden capacity drop and serious polarization in the voltage plots after 60 cycles (Fig. 6(e)), where the ever-deteriorating Li–GPE interface would be one of the main reasons. These results were also proved by the results of EIS measurements for the NCM||GPE||Li and NCM||GPE||$Li/Li_{22}Sn_5/LiF$ cells before and after cycling. As shown in Fig. 6(f), the initial internal resistance (composed of the interfacial resistance and the charge-transfer resistance) for the NCM||GPE||$Li/Li_{22}Sn_5/LiF$ cell was only 130 Ω, much less than 350 Ω for the NCM||GPE||Li cell before cycling. After 50 cycles, the interfacial resistance of the NCM||GPE||Li cell rapidly increased to 700 Ω, while a low value of 200 Ω remained for the NCM||GPE||Li/$Li_{22}Sn_5$/LiF cell under the same test condition (Fig. S20 in the ESM). The significantly increased interfacial resistance was mainly attributable to the emergence of caves on Li surface by uneven dissolution of active Li and nonuniform Li deposition, which continuously deteriorated the interface contact between the Li electrode and the GPE upon cycling. This phenomenon verified that the integrating GPE with the Li/$Li_{22}Sn_5$/LiF electrode effectively inhibited the interfacial polarization upon cycling by the stable interphase structure with low resistance, and improved electrochemical/chemical interfacial stability. It was worth mentioning that the smaller charge-transfer resistance for NCM||GPE||Li/$Li_{22}Sn_5$/LiF cell should partially result from robust $Li_{22}Sn_5$ framework in composite electrode, which was regarded beneficial for accelerating ion transport and stabilizing electrode structure [28–30]. Benefiting from the integration of ionically conductive Li/$Li_{22}Sn_5$/LiF anode and GPE with superior contact (Fig. 6(g)), the NCM||GPE||Li/$Li_{22}Sn_5$/LiF cell delivered a specific capacity of 108.4 $mAh·g^{-1}$ even at the high rate of 4 C, much higher than 77.5 $mAh·g^{-1}$ for the NCM||GPE||Li cell (Fig. 6(h)).

4 Conclusions

In summary, we proposed the improvement of interfacial contact and stability between Li metal anode and GPE by *in situ* catalytic polymerization on anode surface by using functional component of composite anode as the catalyst. We demonstrated that SnF_2 in the Li/$Li_{22}Sn_5$/LiF composite foil electrode initiated the ring-opening polymerization of DOL-base electrolyte on the surface of the electrode, rendering a close interfacial contact between GPE and composite electrode, which was quite different from the *in situ* polymerization of GPE with only catalyst in the bulk of liquid precursor. Together with the merits of robust $Li_{22}Sn_5$ framework with high ionic conductivity and protective LiF component of the composite anode, the Li/$Li_{22}Sn_5$/LiF electrode with *in situ* polymerization of polymer electrolyte on its surface enabled the symmetric cell with long-term electrochemical cyclability over 500 h and a low hysteresis of 25 mV, and full cell pairing NCM cathode with a remarkable capacity retention of 85.7% for 100 cycles at 0.5 C in the potential range of 2.8–4.3 V. The approach employed here, involving the *in situ* polymerization of the gel polymer electrolyte on electrode surface, could be extrapolated to other instances of *in situ* polymerization of various gel polymer electrolytes, facilitated by the embedment of a catalyst into electrode surface. And, the *in situ* catalytic polymerization of GPE on anode surface represents an alternative approach for improving the anode interfacial stability of rechargeable Li metal batteries, exhibits potential compatibility with the current battery fabrication process, and thus is promising for practical application.

Acknowledgments

This work was supported by the National Natural Science Foundation of China (Nos. 52272207 and 62204173). The authors would like to thank the Analytical and Testing Center of Huazhong University of Science and Technology for providing the facilities to carry out the characterizations.

Electronic Supplementary Material: Supplementary material (characterizations including SEM images, XRD patterns, EDS mapping image, and Raman spectra, as well as corresponding optical photos and electrochemical tests for the prepared samples, etc.) is available in the online version of this article at https://doi.org/10.1007/s12274-024-6463-2.

References

[1] Liu, J.; Bao, Z. N.; Cui, Y.; Dufek, E. J.; Goodenough, J. B.; Khalifah, P.; Li, Q. Y.; Liaw, B. Y.; Liu, P.; Manthiram, A. et al. Pathways for practical high-energy long-cycling lithium metal batteries. *Nat. Energy* **2019**, *4*, 180–186.

[2] Meng, Y. S.; Srinivasan, V.; Xu, K. Designing better electrolytes. *Science* **2022**, *378*, eabq3750.

[3] Li, M.; Wang, C. S.; Chen, Z. W.; Xu, K.; Lu, J. New concepts in electrolytes. *Chem. Rev.* **2020**, *120*, 6783–6819.

[4] Zhang, Z. L.; Jin, Y.; Zhao, Y.; Xu, J.; Sun, B.; Liu, K.; Lu, H. F.; Lv, N. W.; Dang, Z. M.; Wu, H. Homogenous lithium plating/stripping regulation by a mass-producible Zn particles modified Li-metal composite anode. *Nano Res.* **2021**, *14*, 3999–4005.

[5] Ye, L. H.; Li, X. A dynamic stability design strategy for lithium metal solid state batteries. *Nature* **2021**, *593*, 218–222.

[6] Hu, Y. R.; Zhong, Y. R.; Qi, L. M.; Wang, H. L. Inorganic/polymer hybrid layer stabilizing anode/electrolyte interfaces in solid-state Li metal batteries. *Nano Res.* **2020**, *13*, 3230–3234.

[7] Vu, T. T.; Cheon, H. J.; Shin, S. Y.; Jeong, G.; Wi, E.; Chang, M. Hybrid electrolytes for solid-state lithium batteries: Challenges, progress, and prospects. *Energy Storage Mater.* **2023**, *61*, 102876.

[8] Lennartz, P.; Paren, B. A.; Herzog-Arbeitman, A.; Chen, X. C.; Johnson, J. A.; Winter, M.; Shao-Horn, Y.; Brunklaus, G. Practical considerations for enabling Li|polymer electrolyte batteries. *Joule* **2023**, *7*, 1471–1495.

[9] Chen, A. L.; Qian, Y. S.; Zheng, S. J.; Chen, Y. Y.; Ouyang, Y.; Mo, L. L.; Xu, Z. L.; Miao, Y. E.; Liu, T. X. *In-situ* constructed polymer/alloy composite with high ionic conductivity as an artificial solid electrolyte interphase to stabilize lithium metal anode. *Nano Res.* **2023**, *16*, 3888–3894

[10] Zhao, Q.; Liu, X. T.; Stalin, S.; Khan, K.; Archer, L. A. Solid-state polymer electrolytes with in-built fast interfacial transport for secondary lithium batteries. *Nat. Energy* **2019**, *4*, 365–373.

[11] Xiang, J. W.; Zhang, Y.; Zhang, B.; Yuan, L. X.; Liu, X. T.; Cheng, Z. X.; Yang, Y.; Zhang, X. X.; Li, Z.; Shen, Y. et al. A flame-retardant polymer electrolyte for high performance lithium metal batteries with an expanded operation temperature. *Energy Environ. Sci.* **2021**, *14*, 3510–3521.

[12] Geng, Z.; Huang, Y. L.; Sun, G. C.; Chen, R. S.; Cao, W. Z.; Zheng, J. Y.; Li, H. *In-situ* polymerized solid-state electrolytes with stable cycling for Li/$LiCoO_2$ batteries. *Nano Energy* **2022**, *91*, 106679

[13] Liu, F. Q.; Wang, W. P.; Yin, Y. X.; Zhang, S. F.; Shi, J. L.; Wang, L.; Zhang, X. D.; Zheng, Y.; Zhou, J. J.; Li, L. et al. Upgrading traditional liquid electrolyte via *in situ* gelation for future lithium metal batteries. *Sci. Adv.* **2018**, *4*, eaat5383.

[14] Zhao, C. Z.; Zhao, Q.; Liu, X. T.; Zheng, J. X.; Stalin, S.; Zhang, Q.; Archer, L. A. Rechargeable lithium metal batteries with an in-built solid-state polymer electrolyte and a high voltage/loading Ni-rich layered cathode. *Adv. Mater.* **2020**, *32*, 1905629.

[15] Sarkar, S.; Chen, B. W.; Zhou, C. T.; Shirazi, S. N.; Langer, F.; Schwenzel, J.; Thangadurai, V. Synergistic approach toward developing highly compatible garnet–liquid electrolyte interphase in hybrid solid-state lithium-metal batteries. *Adv. Energy Mater.* **2023**, *13*, 2203897.

[16] Li, W.; Gao, J.; Tian, H. Y.; Li, X. L.; He, S.; Li, J. P.; Wang, W. L.; Li, L.; Li, H.; Qiu, J. S. et al. SnF_2-catalyzed formation of polymerized dioxolane as solid electrolyte and its thermal decomposition behavior. *Angew. Chem., Int. Ed.* **2021**, *61*, e202114805.

[17] Li, G. C.; Duan, X. R.; Liu, X. T.; Zhan, R. M.; Wang, X. C.; Du, J. M.; Chen, Z. H.; Li, Y. J.; Cai, Z.; Shen, Y. et al. Locking active Li metal through localized redistribution of fluoride enabling stable Li-metal batteries. *Adv. Mater.* **2023**, *35*, 2207310.

[18] Liu, S. F.; Ji, X.; Yue, J.; Hou, S.; Wang, P. F.; Cui, C. Y.; Chen, J.; Shao, B. W.; Li, J. R.; Han, F. D. et al. High interfacial-energy interphase promoting safe lithium metal batteries. *J. Am. Chem. Soc.* **2020**, *142*, 2438–2447.

[19] Wu, C.; Huang, H. F.; Lu, W. Y.; Wei, Z. X.; Ni, X. Y.; Sun, F.; Qing, P.; Liu, Z. J.; Ma, J. M.; Wei, W. F. et al. Mg doped Li-LiB

alloy with *in situ* formed lithiophilic LiB skeleton for lithium metal batteries. *Adv. Sci.* **2020**, *7*, 1902643.

[20] Wang, J. X.; Ye, Y. D.; Zhou, H. M.; Zhang, W.; Sun, Z. W.; Zhu, J. W.; Jin, H. C.; Xie, H. Y.; Huang, H. L.; Cui, Y. et al. Regulating Li transport in Li-magnesium alloy for dendrite free Li metal anode. *Nano Res.* **2023**, *16*, 8338–8344.

[21] Gao, J. L.; Chen, C. J.; Dong, Q.; Dai, J. Q.; Yao, Y. G.; Li, T. Y.; Rundlett, A.; Wang, R. L.; Wang, C. W.; Hu, L. B. Stamping flexible Li alloy anodes. *Adv. Mater.* **2021**, *33*, 2005305.

[22] Jiang, F. N.; Yang, S. J.; Cheng, X. B.; Yuan, H.; Liu, L.; Huang, J. Q.; Zhang, Q. An interface-contact regulation renders thermally safe lithium metal batteries. *eTransportation* **2023**, *15*, 100211.

[23] Liu, M.; Zhang, J. F.; Sun, Z.; Huang, L.; Xie, T.; Wang, X. W.; Wang, D.; Wu, Y. P. Dual mechanism for sodium based energy storage. *Small* **2023**, *19*, 2206922.

[24] Li, G. C.; Yang, Q. P.; Chao, J. L.; Zhang, B.; Wan, M. T.; Liu, X. X.; Mao, E. Y.; Wang, L.; Yang, H.; Seh, Z. W. et al. Enhanced processability and electrochemical cyclability of metallic sodium at elevated temperature using sodium alloy composite. *Energy Storage Mater.* **2021**, *35*, 310–316.

[25] Li, Y. J.; Mao, E. Y.; Min, Z. W.; Cai, Z.; Chen, Z. H.; Fu, L.; Duan, X. R.; Wang, L. Y.; Zhang, C.; Lu, Z. H. et al. Hybrid polymer-alloy-fluoride interphase enabling fast ion transport kinetics for low-temperature lithium metal batteries. *ACS Nano* **2023**, *19*, 19459–19469.

[26] Zhang, N.; Li, J.; Li, H. Y.; Liu, A.; Huang, Q.; Ma, L.; Li, Y.; Dahn, J. R. Structural, electrochemical, and thermal properties of nickel-rich $LiNi_xMn_yCo_zO_2$ materials. *Chem. Mater.* **2018**, *30*, 8852–8860.

[27] Liang, J. Y.; Zhang, X. D.; Zhang, Y.; Huang, L. B.; Yan, M.; Shen, Z. Z.; Wen, R.; Tang, J. L.; Wang, F. Y.; Shi, J. L. et al. Cooperative shielding of Bi-electrodes via *in situ* amorphous electrode–electrolyte interphases for practical high-energy lithium-metal batteries. *J. Am. Chem. Soc.* **2021**, *143*, 16768–16776.

[28] He, Y. F.; Zhang, M. Y.; Wang, A. P.; Zhang, B.; Pham, H.; Hu, Q.; Sheng, L.; Xu, H.; Wang, L.; Park, J. et al. Regulation of dendrite-free Li plating via lithiophilic sites on lithium−alloy surface. *ACS Appl. Mater. Interfaces* **2022**, *14*, 33952–33959.

[29] Li, Y. J.; Feng, X.; Lieu, W. Y.; Fu, L.; Zhang, C.; Ghosh, T.; Thakur, A.; Wyatt, B. C.; Anasori, B.; Liu, W. et al. MXene-based anode-free magnesium metal battery. *Adv. Funct. Mater.* **2023**, *33*, 2303067.

[30] Shi, Y. C.; Fu, J. P.; Hui, K. L.; Liu, J.; Gao, C.; Chang, S. Q.; Chen, Y. J.; Gao, X.; Gao, T.; Qu, L. G. et al. Promoting the electrochemical properties of yolk–shell-structured CeO_2 composites for lithium-ion batteries. *Microstructures* **2021**, *1*, 2021005.